

Stellar rotation and the extended main sequence turnoff in the open cluster NGC 5822

WEIJIA SUN,¹ RICHARD DE GRIJS,^{2,3} LICAI DENG,^{4,5,6} AND MICHAEL D. ALBROW⁷

¹*Kavli Institute for Astronomy & Astrophysics and Department of Astronomy, Peking University, Yi He Yuan Lu 5, Hai Dian District, Beijing 100871, China*

²*Department of Physics and Astronomy, Macquarie University, Balaclava Road, Sydney, NSW 2109, Australia*

³*International Space Science Institute–Beijing, 1 Nanertiao, Hai Dian District, Beijing 100190, China*

⁴*Key Laboratory for Optical Astronomy, National Astronomical Observatories, Chinese Academy of Sciences, 20A Datun Road, Chaoyang District, Beijing 100012, China*

⁵*School of Astronomy and Space Science, University of the Chinese Academy of Sciences, Huairou 101408, China*

⁶*Department of Astronomy, China West Normal University, Nanchong 637002, China*

⁷*School of Physical and Chemical Sciences, University of Canterbury, Private Bag 4800, Christchurch, New Zealand*

ABSTRACT

The origin of extended main sequence turnoffs (eMSTOs) in intermediate-age (1 – 3 Gyr) clusters is one of the most intriguing questions in current star cluster research. Unlike the split main sequences found in some globular clusters, which are caused by bimodal populations in age and/or chemical abundances, eMSTOs are believed to be owing to stellar rotation. We present a spectroscopic survey of MSTO stars in a nearby, intermediate-age (0.9 Gyr), low mass ($\sim 1.7 \times 10^3 M_{\odot}$) Galactic open cluster, NGC 5822. We derive a clean sample of member stars based on *Gaia* proper motions and parallaxes and confirm the existence of an eMSTO. Using medium-resolution ($R \sim 4000$) Southern African Large Telescope (SALT) spectra, we derive the rotational velocities of 24 member stars (representing 20% completeness around the eMSTO region) and find that the loci of the main sequence stars in the eMSTO region show a clear correlation with the projected rotational velocities in the sense that fast rotators are located on the red side of the eMSTO and slow rotators are found on the blue side. By comparison with a synthetic cluster model, we show that the stellar rotational velocities and the eMSTO of NGC 5822 can be well reproduced and we conclude that stellar rotation is the main cause of the eMSTO in NGC 5822.

Keywords: stars: rotation — open clusters and associations: individual: NGC 5822 — galaxies: star clusters: general.

1. INTRODUCTION

The extended main sequence turnoff (eMSTO) phenomenon—i.e., the notion that the main sequence turnoff (MSTO) in the color–magnitude diagram (CMD) is much wider than the prediction from single stellar population modeling—first discovered in NGC 1846 by Mackey & Broby Nielsen (2007), is a common feature found in a large fraction of young and intermediate-age (≤ 2 Gyr) massive Large and Small Magellanic Cloud clusters (e.g. Mackey et al. 2008; Milone et al. 2009; Goudfrooij et al. 2011; Li et al. 2014b; Correnti et al. 2017; Milone et al. 2015).

In the past few years, our understanding of the eMSTO phenomenon in these clusters has been enriched and enhanced significantly. Rather than owing to intrinsic age spreads, stellar rotation is believed to play an important role in shaping the morphology of the eMSTO (e.g., Li et al. 2014a; Niederhofer et al. 2015; Bastian & De Mink 2009). This theory is further reinforced by multiple lines of photometric and spectroscopic evidence. Using narrow-band photometry, Bastian et al. (2017) detected a large fraction (~ 30 –60%) of Be stars in the MSTO regions of NGC 1850 (~ 80 Myr) and NGC 1856 (~ 280 Myr), favoring the interpretation that their split main sequences are caused by the effects of fast rotators. Similar mechanisms were later confirmed in NGC 1866 (~ 200 Myr) and NGC 1818 (~ 40 Myr) through high-resolution spectroscopic surveys, suggesting that these clusters host a blue main sequence composed of slow rotators and a red one composed of fast rotators (Dupree et al. 2017; Marino et al. 2018b).

Aided by *Gaia* Data Release 2 (DR2), we can derive ‘clean’ samples of open clusters in the Milky Way free of contamination by field stars (Cantat-Gaudin et al. 2018). The discovery of eMSTOs in Galactic open clusters, similar

to those observed in Magellanic Cloud clusters, has opened up a new chapter in our comprehension of the formation of eMSTOs and the evolution of open clusters. [Cordoni et al. \(2018\)](#) found the existence of eMSTOs in all 12 open clusters younger than ~ 1.5 Gyr they analyzed (including NGC 5822), suggesting that eMSTOs are a common feature of intermediate-age clusters in the Milky Way and that they are regulated by the same mechanism as that operating in Magellanic Cloud clusters. The understanding of open clusters, which used to be considered prototypes of a single stellar population, encountered a significant upheaval due to the discovery of eMSTOs in Galactic open clusters. It has been reported that stars exhibit a wide range of rotation rates both in the field ([Huang et al. 2010](#)) and in open clusters ([Huang & Gies 2006](#)). A number of studies have explored the effect of stellar rotation on the CMD around the MSTO region ([Brandt & Huang 2015a,b,c](#)). However, the direct connection between the stellar rotation rates of MSTO stars and their loci in the CMD was only revealed recently. [Bastian et al. \(2018\)](#) used Very Large Telescope/FLAMES spectroscopy of 60 cluster members in NGC 2818, an 800 Myr open cluster, to measure the stellar rotational velocities and found that stars exhibiting high rotational velocities are located on the red side of the eMSTO and those rotating slowly on the blue side, in agreement with the prediction of the stellar rotation scenario. [Marino et al. \(2018a\)](#) also reported that the multiple sequences they found in the young cluster NGC 6705 correspond to stellar populations with different rotation rates.

In this paper, we present a spectroscopic survey of MSTO stars in the nearby (~ 760 pc) intermediate-age (0.9 Gyr) open cluster NGC 5822. We find the presence of an eMSTO in this cluster and verify that it is not an artifact caused by differential extinction. The loci of the main sequence stars in the eMSTO region show a clear correlation with the projected rotational velocities, with fast rotators lying on the red side of the eMSTO and slow rotators on the blue side. By comparison with a synthetic cluster within the framework of stellar rotation, we argue that the observed morphology of the eMSTO in the CMD can be properly explained by the model and that stellar rotation is likely the main contributor to the eMSTO morphology in NGC 5822.

This article is organized as follows. In Section 2 we present the observations, data reduction procedures, and membership determination. Section 3 reports our main results, showing a strong correlation between the stellar rotation rates and their loci in the CMD region covered by the eMSTO. A discussion and our conclusions are summarized in Section 4.

2. DATA REDUCTION AND ANALYSIS

2.1. Spectroscopic data

We selected spectroscopic candidates in NGC 5822 using the photometric survey in the *UBVI* and *uvbyCaH β* systems undertaken by [Carraro et al. \(2011\)](#). These broad-band observations were obtained with the Y4KCAM camera mounted on the Cerro Tololo Inter-American Observatory (CTIO) 1 m telescope and the intermediate- and narrow-band imaging was carried out using the CTIO 0.9 m telescope. Through a cross-correlation with the UCAC3 database ([Zacharias et al. 2000](#)), these authors derived 136 probable photometric members and 322 probable non-members.

We obtained spectroscopic observations with the Southern African Large Telescope (SALT; [Buckley et al. 2006](#)) equipped with the Robert Stobie Spectrograph (RSS) using its multi-object spectroscopy (MOS) capability over 9 nights from 2018 February 8/9 to 2018 August 14/15 under programs 2017-2-SCI-038 and 2018-1-SCI-006. Six masks were designed to cover 88 stars (including repetitions) in NGC 5822 as part of program 2017-2-SCI-038, with three masks observed for the second time the following semester (see Table 1). The PG2300 grating was used with a 1 arcsec wide short slit binned 2×2 , offering a nominal spectral resolution of ~ 4000 with a per-pixel resolution of 0.33 \AA at a central wavelength of 4884.4 \AA . Regular bias, argon arc lamp, and quartz lamp flat field calibration frames were taken as part of normal SALT operations. We used the PySALT package ([Crawford et al. 2010](#)) to perform the primary reduction and wavelength calibration. For all of our samples, we obtained spectra with a signal-to-noise ratio (SNR) per pixel in excess of 200.

2.2. Membership determination

We exploited the *Gaia* DR2 ([Gaia Collaboration et al. 2016, 2018](#)) to analyze the stellar photometry, proper motions, and parallaxes, and to perform membership determination in the NGC 5822 field. First, we acquired the stellar catalog from the *Gaia* database within 2.5 times the cluster radius ($35'$; [Dias et al. 2002](#)). In the vector-point diagram (VPD) of stellar proper motions, NGC 5822 showed a clear concentration centered at $(\mu_\alpha \cos \theta, \mu_\delta) \approx (-7.44, -5.52) \text{ mas yr}^{-1}$. The other overdensity located at $(\mu_\alpha \cos \theta, \mu_\delta) \approx (-3.67, -2.52) \text{ mas yr}^{-1}$ corresponds to a nearby cluster, NGC 5823. Then, we derived the quantity $\mu_R = \sqrt{(\mu_\alpha \cos \theta - \langle \mu_\alpha \cos \theta \rangle)^2 + (\mu_\delta - \langle \mu_\delta \rangle)^2}$ and applied a cut of

$\mu_R = 0.4 \text{ mas yr}^{-1}$ to conduct our primary membership selection. Next, we placed a further constraint on the parallaxes by estimating the mean parallax of the proper-motion-selected stars ($\langle \varpi \rangle = 1.18 \text{ mas yr}^{-1}$) and adopted stars with parallaxes within $0.115 \text{ mas yr}^{-1}$ as cluster members. Note that this approach is slightly different from that adopted by [Cordoni et al. \(2018\)](#), in the sense that we adopted a straight cut in both μ_R and ϖ rather than applying different selection criteria for stars of different brightnesses. One reason for this approach is that NGC 5822 is sufficiently close that its member stars can be easily separated from field stars using parallaxes (see the top right-hand panel of Fig. 1). On the other hand, the limited number of stars in NGC 5822 makes it hard to reliably calculate the corresponding rms for each magnitude bin. Since we did not set out to compile a homogeneous database for multiple clusters, our approach is suitable for our analysis of this single cluster. We present the spatial distribution as well as the CMD of the member stars of NGC 5822, together with all stars in the field, in the bottom panels of Fig. 1. We present the CMD of NGC 5822 color-coded by the stellar classifications based on their loci in Fig. 2. Member stars classified as MSTO, MS, and giant stars are marked as green squares, blue triangles, and red diamonds, respectively. Member stars with spectroscopic data are presented using solid markers and field stars with spectroscopic data are shown as gray circles. Following decontamination of the field stars, 24 member stars (21 MSTO and 3 MS stars) were left in our observational sample; 13 member stars were observed a second time. We estimate that the total number of member MSTO stars in this cluster is ~ 107 , suggesting that the completeness of our observed sample is around 20% in the eMSTO region.

This cluster shows a clear eMSTO feature around $G \sim 11.5 \text{ mag}$. To further demonstrate that this is not an artifact owing to residual differential reddening, we estimated the degree of the spatial variation of the reddening and found that its influence is negligible compared with the extent of the eMSTO. Given its close distance and low Galactic latitude, we found that we could not use a 2D reddening map (e.g. [Schlafly & Finkbeiner 2011](#)) to estimate the differential reddening. Instead, we adopted the method of [Nataf et al. \(2013\)](#), who assumed a two-component model for the distribution of the dust, including the mean density of dust along the plane ρ_D and a scale height H_D . Therefore, the prediction for the reddening in a given direction is given by

$$E(B - V) = \rho_D \int_0^d \exp(-r \sin(|b|)/H) dr, \quad (1)$$

where b represents Galactic latitude and d is the distance derived from the corresponding *Gaia* parallax. The distance was derived from the parallax by implementing the formalism of [Astraatmadja & Bailer-Jones \(2016\)](#). $H = 164 \text{ pc}$ is the dust scale height and $\rho_D = 0.427 \text{ mag kpc}^{-1}$ ([Nataf et al. 2013](#)). The average extinction for cluster members is around $E(B - V) = 0.126 \text{ mag}$ with a standard deviation of $\sigma_{E(B-V)} = 0.004 \text{ mag}$. Using the [Cardelli et al. \(1989\)](#) and [O'Donnell \(1994\)](#) extinction curve with $R_V = 3.1$, we corrected the reddening to the average reddening value. In Fig. 3 we present the CMD of selected cluster member stars before (left) and after (right) our differential reddening

Table 1. Observation Log of the SALT Runs

Mask Name	Programme	α_{J2000}	δ_{J2000}	N^a	Exp. Time (s)	Date (UT)
(1)	(2)	(3)	(4)	(5)	(6)	(7)
NGC5822p2	2017-2-SCI-038	15 ^h 04 ^m 33.43 ^s	−54°26′33.16″	13	600	2018 Feb 8
	2018-1-SCI-006	15 ^h 04 ^m 33.43 ^s	−54°26′33.16″	13	764	2018 Aug 3
NGC5822p3	2017-2-SCI-038	15 ^h 04 ^m 19.43 ^s	−54°16′44.52″	10	600	2018 Apr 26
NGC5822p4	2017-2-SCI-038	15 ^h 03 ^m 11.44 ^s	−54°16′22.93″	11	600	2018 Feb 8
	2018-1-SCI-006	15 ^h 03 ^m 11.44 ^s	−54°16′22.93″	11	764	2018 Jul 30
NGC5822p6	2017-2-SCI-038	15 ^h 03 ^m 09.95 ^s	−54°31′46.39″	9	600	2018 Feb 11
	2018-1-SCI-006	15 ^h 03 ^m 09.95 ^s	−54°31′46.39″	9	764	2018 Aug 14
NGC5822p8	2017-2-SCI-038	15 ^h 05 ^m 10.13 ^s	−54°19′41.91″	7	600	2018 Feb 26
NGC5822p9	2017-2-SCI-038	15 ^h 04 ^m 36.35 ^s	−54°34′51.48″	5	600	2018 Apr 30

^aNumber of science slits in each field.

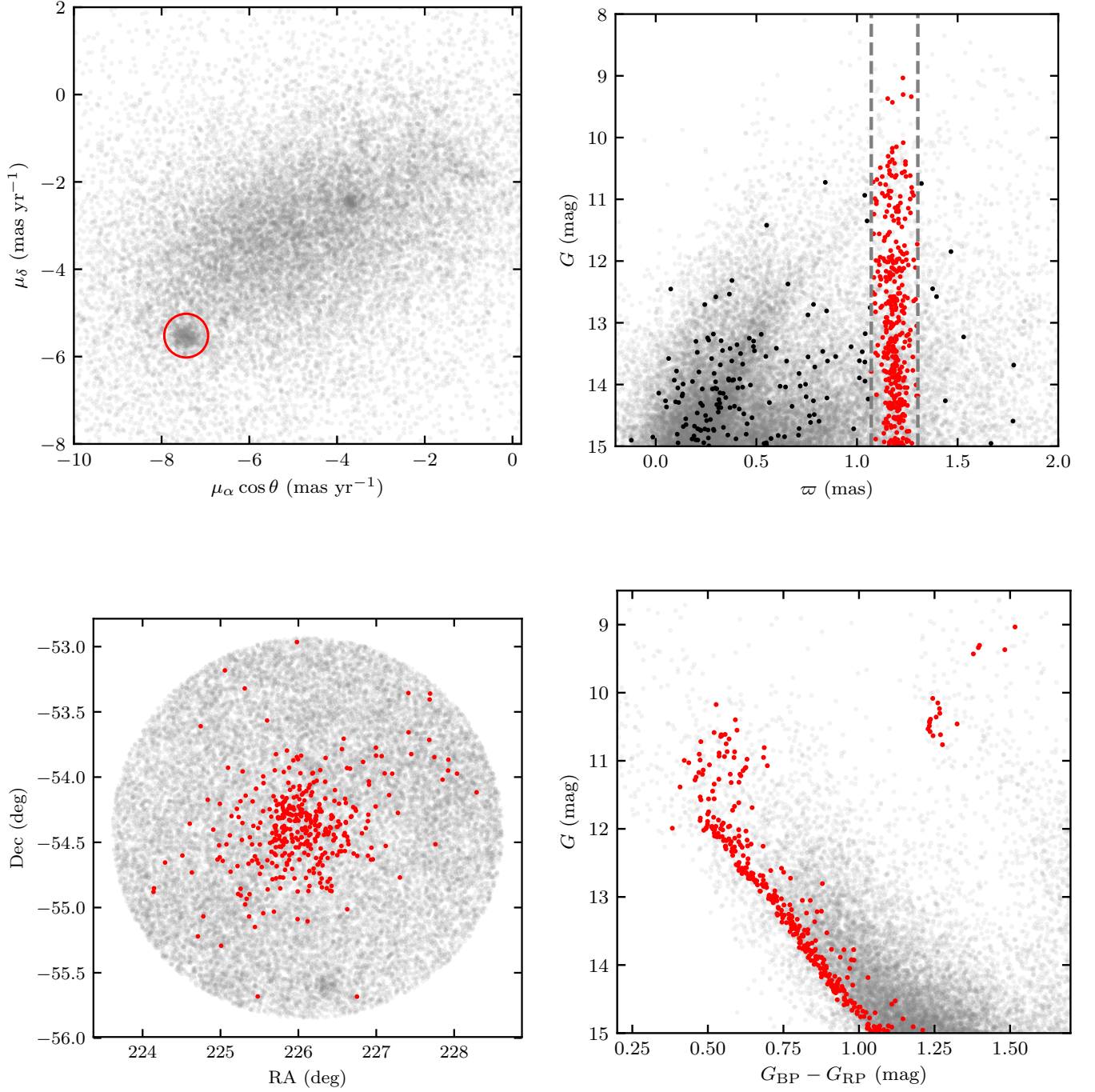


Figure 1. **(top left)** Vector-point diagram of the proper motions for stars brighter than $G = 15$ mag within $87.5'$ of the center of NGC 5822. The red circle shows the primary selection of cluster members. **(top right)** G band vs. parallaxes. The primary members selected from the proper motions are marked as solid dots and the parallax-selected members are marked as red dots. The vertical dashed lines represent the selection criteria applied to the parallaxes. **(bottom left)** Spatial distribution of stars selected, with cluster members highlighted as red points. **(bottom right)** CMD of all stars in the field (gray dots) and member stars of NGC 5822 (red solid dots). The eMSTO is visible around $G \sim 11.5$ mag.

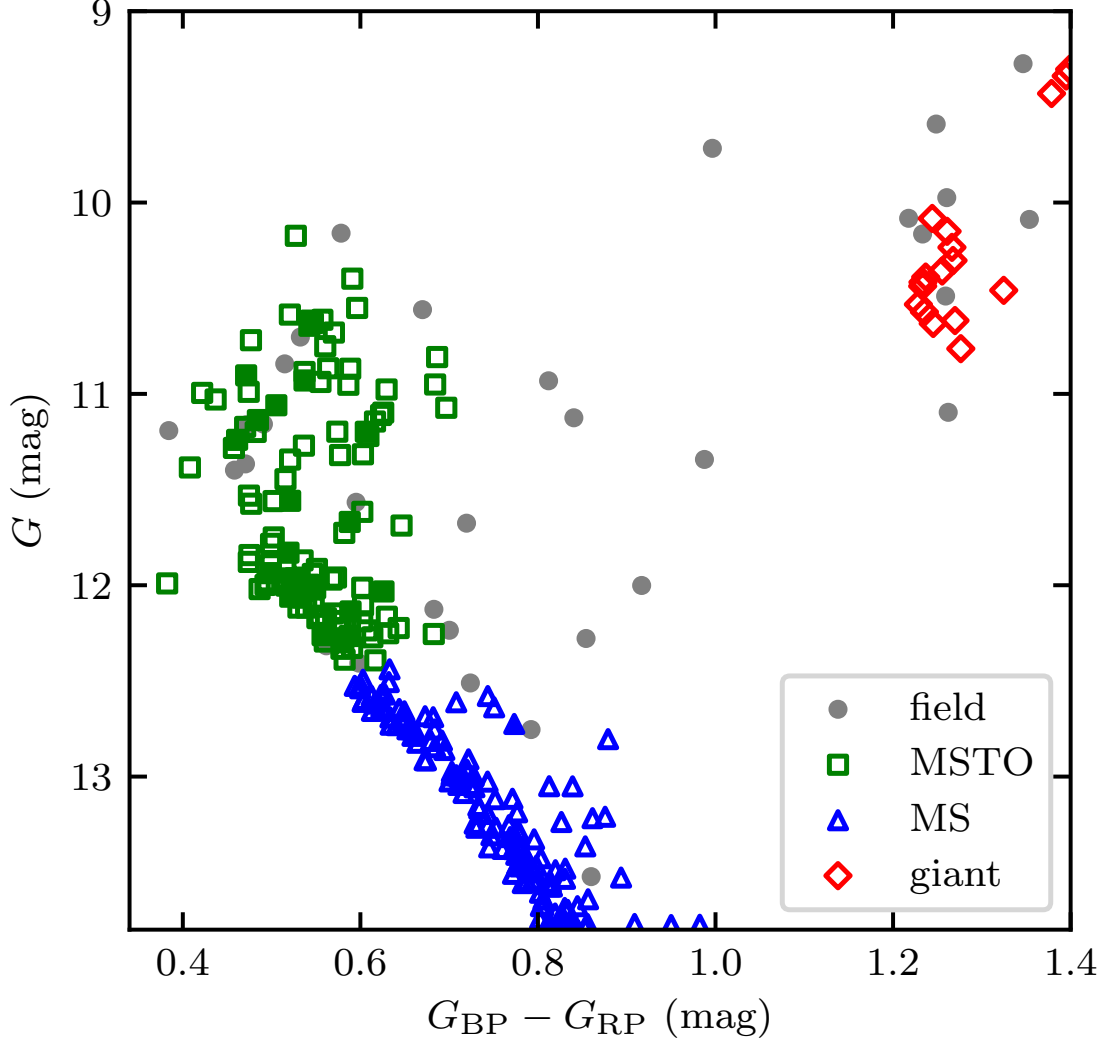


Figure 2. CMD of NGC 5822 color-coded by the stellar classifications based on their loci. Member stars classified as MSTO, MS, and giant stars are marked as green squares, blue triangles, and red diamonds, respectively. Member stars with spectroscopic data are presented using solid markers and field stars with spectroscopic data are shown as gray circles.

correction. A visual inspection suggests that the morphology of the CMD remains unchanged and the eMSTO still exists after having applied this correction.

We used the Padova group’s PARSEC 1.2S isochrones (Bressan et al. 2012) to perform our CMD fits based on visual matching. Cordoni et al. (2018) derived an age of ~ 1 Gyr and a solar-like metallicity ($Z_{\odot} = 0.0152$). Our best fit agrees with these results (Fig. 3). The best-fitting isochrone has an age of 0.9 Gyr for $Z = 0.017$ and a distance of ~ 760 pc. The binary sequence is clearly visible in the CMD and Cordoni et al. (2018) estimated the fraction of unresolved binaries with $q > 0.7$ at 0.131.

2.3. Rotational velocities

The projected rotational velocities were measured by fitting the absorption line profiles of $H\beta$ and the Mg I triplet. We compiled a library of high-resolution synthetic stellar spectra with effective temperatures, T_{eff} , ranging from 5000 K to 8000 K (in steps of 100 K), surface gravities from $\log g = 3.5$ to $\log g = 5.0$ (in steps of 0.1), and metallicities from $[\text{Fe}/\text{H}] = -1.0$ to $[\text{Fe}/\text{H}] = 1.0$ dex (in steps of 0.5 dex) from the Pollux database (Palacios et al. 2010). We applied the latest ATLAS12 model atmospheres (Kurucz 2005) where blanketed model atmospheres handle line opacity in stellar atmospheres using the Opacity Sampling technique. The models assume a plane parallel geometry, hydrostatic

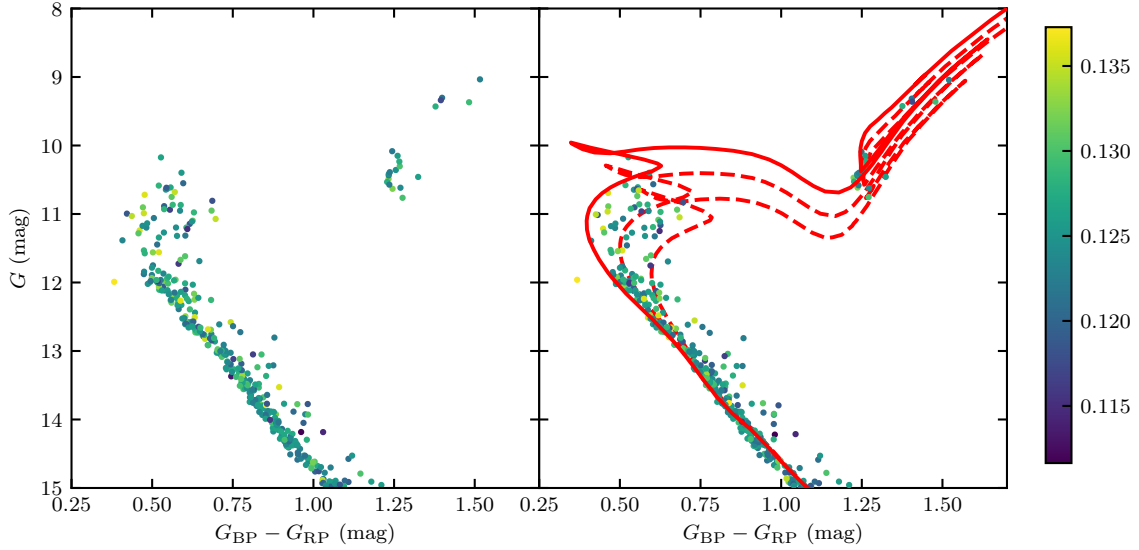


Figure 3. Comparison of the CMD of selected cluster member stars before (left) and after (right) differential reddening correction. Different colors represent different extinctions $E(B - V)$. The best-fitting isochrone for the bulk stellar population is shown in the right-hand panel as a red solid line. The best-fitting isochrone (red solid line) has an age of 0.9 Gyr with $Z = 0.017$ and a distance modulus of around 9.4 (~ 760 pc). Isochrones for ages of $\log(t \text{ yr}^{-1}) = 9.05$ and 9.15 are also overplotted (red dashed lines).

and radiative equilibrium, as well as local thermodynamic equilibrium. The microturbulent velocity was fixed to 2 km s^{-1} for all models. Synthetic spectra were then generated using the SYNSPEC tool (Hubeny & Lanz 1992). Each model spectrum was convolved with the rotational profile for a given rotational velocity and implemented with an instrumental broadening as well as a radial velocity shift. Given that the light enters through off-axis slits (in the dispersion direction) in the MOS, the actual resolution may vary from slit to slit and from mask to mask. Therefore we adopted the full width at half maximum (FWHM) of the corresponding arc lines as an indicator of the instrumental broadening effect. Then, we used the Markov chain Monte Carlo (emcee; Foreman-Mackey et al. 2013) method to sample the five-dimensional parameter space ($v \sin i$, v_r , T_{eff} , $\log g$, $[\text{Fe}/\text{H}]$) to employ a χ^2 minimization. For each of the 3000 runs of the MCMC procedures, χ^2 values and their associated probabilities $e^{-\chi^2/2}$ were stored. Probability distributions were then generated by projecting the sum of the probabilities onto the dimension considered. A Gaussian fit to the distribution provides its width σ , which we adopt as the uncertainty.

To estimate the influence of instrumental broadening on the determination of the rotational velocities, we generated a set of mock spectra by sampling the projected rotational velocities $v \sin i$ from 20 km s^{-1} to 200 km s^{-1} , assuming a uniform SNR = 200 and a reasonable uncertainty for the instrumental broadening ($\sigma_{\text{FWHM}} = 0.1 \text{ \AA}$), and we measured the best-fitting parameters from those mock spectra. We repeated this procedure 100 times and estimated the median values and the 68th percentiles of the velocity distribution. In Fig. 4 we present a comparison of the rotational velocities of the mock data with those derived through profile fitting. The blue shadowed region corresponds to 1σ and the one-to-one relation is indicated by an orange solid line. Given the intermediate spectral resolution, it is hard to differentiate the effect of rotational from instrumental broadening for slow rotators. Therefore, we defined the detection limit of the rotational velocity to be the velocity where its uncertainty is around half of the actual value and, for slow rotators with $v \sin i \leq 55 \text{ km s}^{-1}$, the uncertainties of the measurements are comparable to their actual values, while the uncertainty is less than 5% and 3% for the mock spectra with $v \sin i \geq 100 \text{ km s}^{-1}$ and $v \sin i \geq 150 \text{ km s}^{-1}$, respectively.

3. EXTENDED MSTOS AND STELLAR ROTATION

The eMSTO of NGC 5822, if interpreted as an age difference, is around 300 – 350 Myr. Cordoni et al. (2018) estimated the ages of the stars around the eMSTO region by linearly interpolating a grid of isochrones and calculated the FWHM of the cluster’s age distribution, which gives a spread of 270 ± 52 Myr. They also showed that the FWHM

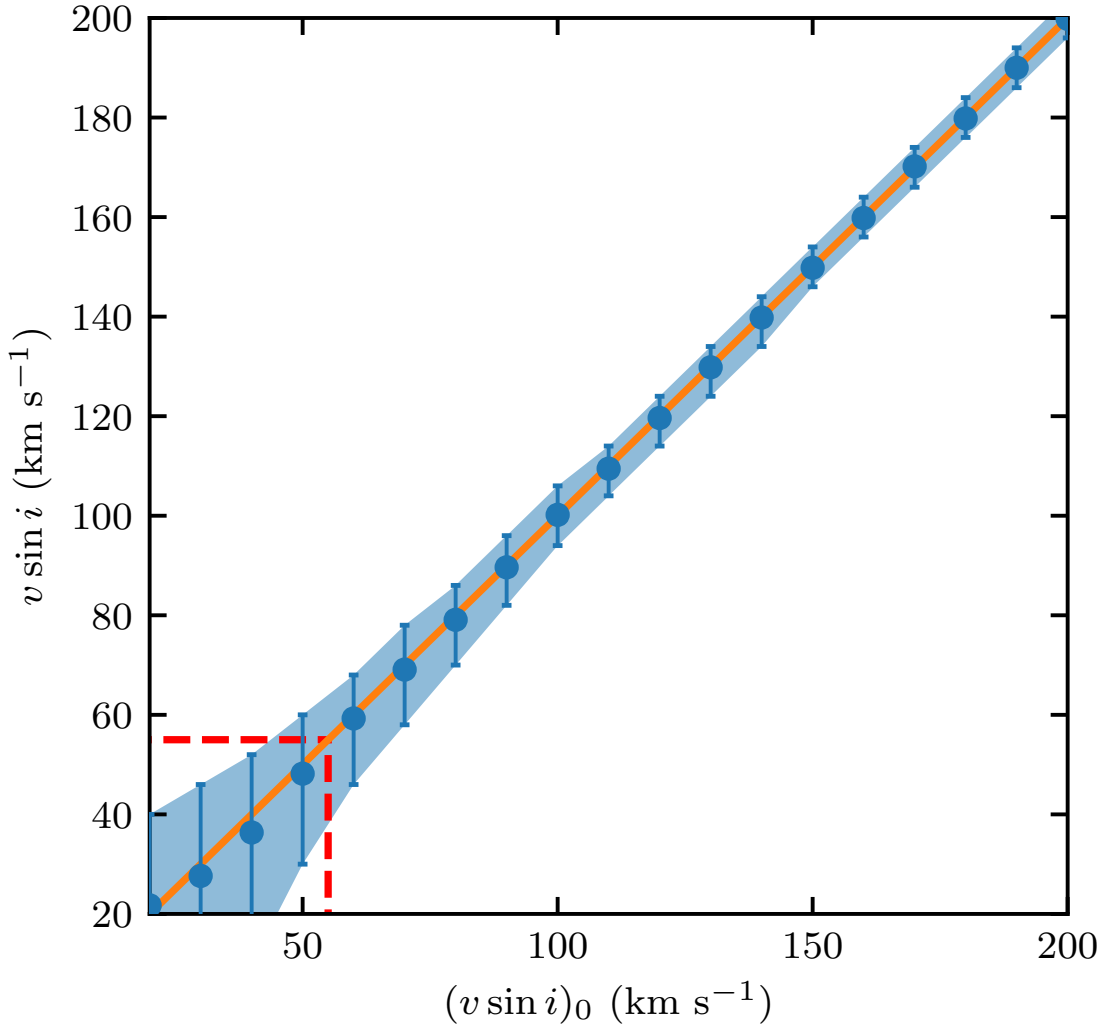


Figure 4. Rotational velocities of the mock data (horizontal axis) vs. rotational velocities derived from profile fitting. The blue shaded region corresponds to 1σ and the one-to-one relation is indicated by an orange solid line. The red dashed lines represent the lower limit of reliable measurements of the rotational velocity (55 km s^{-1}) where the uncertainty is around half of the actual value.

of the NGC 5822 eMSTO follows the correlation between the width of the eMSTO and cluster age applicable within the framework of stellar rotation.

In Fig. 5, we present the CMD of NGC 5822, with the member stars color-coded by their rotational velocities. We found that their loci in the CMD region covered by the eMSTO strongly depend on stellar rotation, in the sense that rapid rotators tend to lie on the red side of the eMSTO while slow rotators are usually found on the blue side. Similar results have also been discovered in young and intermediate-age clusters in the Magellanic Clouds (Dupree et al. 2017; Kamann et al. 2018), as well as in Galactic open clusters (Marino et al. 2018a; Bastian et al. 2018). The stellar structural parameters as well as the inferred projected rotational velocities are listed in Table 2.

We also compared the observed cluster data with a synthetic cluster data set that included the effects of stellar rotation. The synthetic cluster data were derived from the SYCLIST models (Georgy et al. 2013, 2014), assuming a metallicity of $Z = 0.014$, an age of $\log(t \text{ yr}^{-1}) = 8.95$, and a binary fraction of 0.131, with a rotational distribution derived from Huang et al. (2010) and a random rotation axis distribution. The model also accounts for the limb-darkening effect (Claret 2000) as well as for the gravity darkening law of Espinosa Lara & Rieutord (2011). In the left-hand panel of Fig. 6, the synthetic cluster is superposed onto the CMD of NGC 5822 and the eMSTO feature is

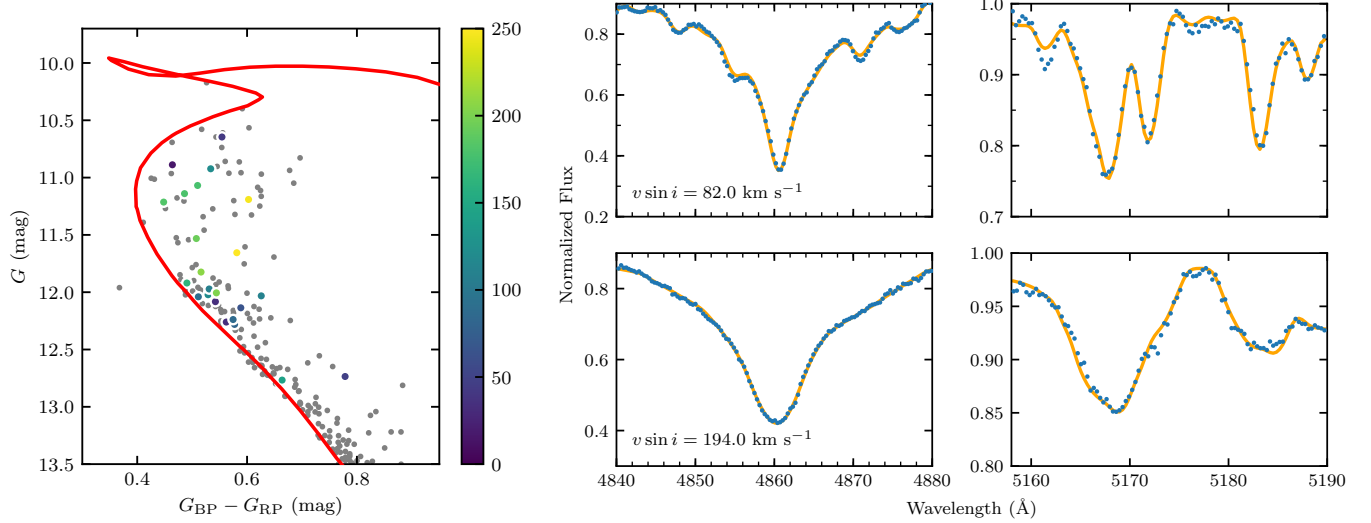


Figure 5. (left) CMD of NGC 5822 with the member stars color-coded by their rotational velocities. The best-fitting isochrone is shown as the red curve. A clear trend between stellar rotation and their loci in the CMD region is seen, in the sense that the rapid rotators (yellow) tend to lie on the red side of the eMSTO while the slow rotators (blue) are usually found on the blue side. (right) Two sample spectra of a slow rotator (top) and a fast rotator (bottom). $H\beta$ and $Mg\ I$ triplets of the same object are shown in the left- and right-hand columns, respectively. For each spectrum, the best-fitting models are presented as orange curves.

well-reproduced and consistent with coeval stellar populations with different rotation rates. The projected rotational velocity of the synthetic cluster follows a similar trend as the real member stars, which become redder as the stellar rotation rates increase. In the middle panel we present a realistic synthetic cluster with a number of stars comparable to that in the observed CMD.

To provide a better comparison with the simulation, we introduced the pseudo-color $\Delta(G_{bp} - G_{rp})$ as the normalized color difference with respect to the blue ridgeline in the direction determining how stellar rotation may change the locus of a star in the CMD (black arrow) to represent the deviation in color which may be caused by stellar rotation. We adopted the blue edge of the synthetic cluster, which represents the population of non-rotating stars, as the fiducial ridgeline. In the right-hand panel of Fig. 6, the $\Delta(G_{bp} - G_{rp})$ vs. $v \sin i$ diagram for all stars with projected rotational velocity measurements is shown, and the gray dots represent the same distribution for the synthetic cluster. We found that most of our targets follow the trend predicted by the stellar rotational model, where the pseudo-color is close to zero for slow rotators and it increases significantly as the rotational velocity increases. Two outliers in the right-hand panel of Fig. 6 (*Gaia* ID: 5887669198096568960 and 5887671397119565312), which have relatively large pseudo-colors compared with their rotational velocities, may result from contamination by binary stars. Since their locations in the CMD coincide with the equal-mass binary sequence, they are likely unresolved binaries, particularly the star with *Gaia* ID 5887671397119565312, whose low mass ($1.2 - 1.3 M_{\odot}$) is close to the minimum mass for large stellar rotation. With such a low mass, stars brake efficiently early on the MS and evolve back to the non-rotating tracks (Georgy et al. 2018). Therefore, stellar rotation is unlikely the cause of such a large shift in color and binary stars might be a plausible explanation of these two outliers.

4. DISCUSSION AND CONCLUSIONS

NGC 5822 is an intermediate-age (0.9 Gyr) Galactic open cluster exhibiting an eMSTO. Through membership determination based on *Gaia* proper motions and parallaxes, we investigated the CMDs of NGC 5822 and confirmed that the eMSTO is unlikely an artifact caused by differential extinction. By exploiting SALT/RSS data, we derived the projected rotational velocities of 24 member stars and found that stellar rotation is strongly correlated with the stellar loci in the CMD in the MSTO region. The red side of the eMSTO is occupied by fast rotators while the blue side is mainly composed of slow rotators. By comparison with a synthetic cluster, we have shown that the eMSTO of

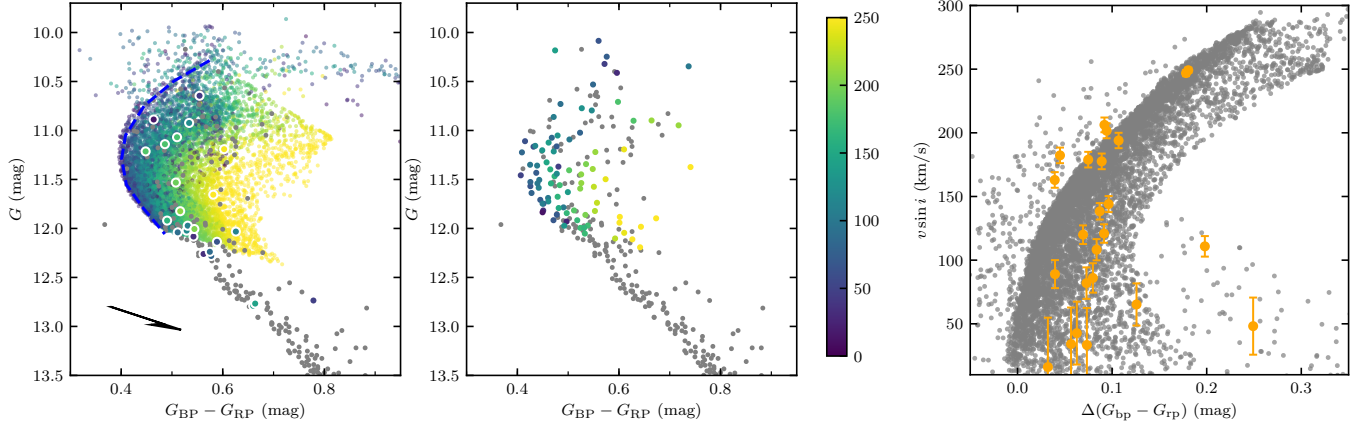


Figure 6. (left) CMD of the observed cluster (gray dots), as well as the synthetic cluster, with colors representing the projected rotational velocities. Larger points with white borders reflect measurements of member stars. The adopted ridgeline is shown as a blue dashed line. The black arrow represents indicates how stellar rotation affects the locus of a star in the CMD. **(middle)** Realistic synthetic cluster with a number of stars comparable to that in the observed CMD. **(right)** Pseudo-color vs. rotational velocity. Stars with projected rotational velocity measurements are marked as orange dots and the synthetic cluster stars are marked as gray dots.

NGC 5822 can be properly reproduced and the rotational velocities of the eMSTO stars follow the same pattern as that predicted by the stellar rotation model.

Combined with NGC 6705 (250 Myr; [Marino et al. 2018a](#)) and NGC 2818 (800 Myr; [Bastian et al. 2018](#)), we have confirmed the correlation between stellar rotation and stellar positions in the eMSTO/split MS in three Galactic open clusters. [Cordoni et al. \(2018\)](#) found that Galactic open clusters also follow the trend between cluster age and the extent of eMSTO seen in Magellanic Cloud clusters ([Yang et al. 2013](#)), suggesting that they should be regulated by a similar mechanism. Split MSs are believed to be composed of two stellar populations characterized by different rotation rates: the blue MS is composed of slow rotators and the red MS is composed of rapid rotators ([Milone et al. 2016](#)). Spectroscopic surveys of the young clusters NGC 1818 ([Marino et al. 2018b](#)) and NGC 6705 ([Marino et al. 2018a](#)) confirmed the existence of slowly and rapidly rotating populations and found that these two subgroups are well separated in projected rotational velocity, with a difference in mean $v \sin i$ greater than 100 km s^{-1} . Meanwhile, in the intermediate-age clusters NGC 2818 ([Bastian et al. 2018](#)) and NGC 5822, such a result is barely seen, which may due to small-number statistics and selection effects. Therefore, we estimated the rotational velocities for all MSTO stars in NGC 5822 based on our synthetic cluster to check the distribution of the stellar rotation rates. On the basis of previous analyses, we argue that the synthetic cluster can properly reproduce the observed results and that it can be taken as a reasonable approximation to the real cluster. Thus, for each member star in the NGC 5822 MSTO region, we inferred the rotational velocities by taking the average velocities of the nearest 50 stars in the synthetic CMD.

The distributions of projected rotational velocity $v \sin i$ and v_{rot} are presented in Fig. 7. We found that the projected rotational velocities show a dip around 150 km s^{-1} , similar to the results for NGC 1818 and NGC 6705. However we suggest that this is an artifact caused by projection effects. In Fig. 7, the ‘slow’ rotators have a peak at 100 km s^{-1} and they have a dearth of stars with $v \sin i \sim 50 \text{ km s}^{-1}$, which is different from the results for the young clusters where the slowly rotating populations have lower mean velocities and do not show a gap in slowly rotating stars. The distribution of the true rotational velocities is also shown in Fig. 7 and the fact that it shows a single peak around 200 km s^{-1} further confirms that the equatorial velocities in NGC 5822 should follow a unimodal distribution. On the other hand, projection effects are unlikely to explain the large difference in projected rotational velocities found in young clusters and the true rotation rates of MSTO stars in young clusters should in all probability show a bimodal distribution given the fact that the split MSs can be separated into distinct sequences in the CMD. Since the typical masses of the split MSs in young clusters ($\geq 2.5 M_{\odot}$) and eMSTOs in intermediate-age clusters ($1.4 M_{\odot} - 2 M_{\odot}$) are different, if a split MS and eMSTO are present in the evolutionary sequence of star clusters, these two distributions of stellar rotation may coexist in the same cluster. This may hint that the stellar rotation distribution in clusters follow

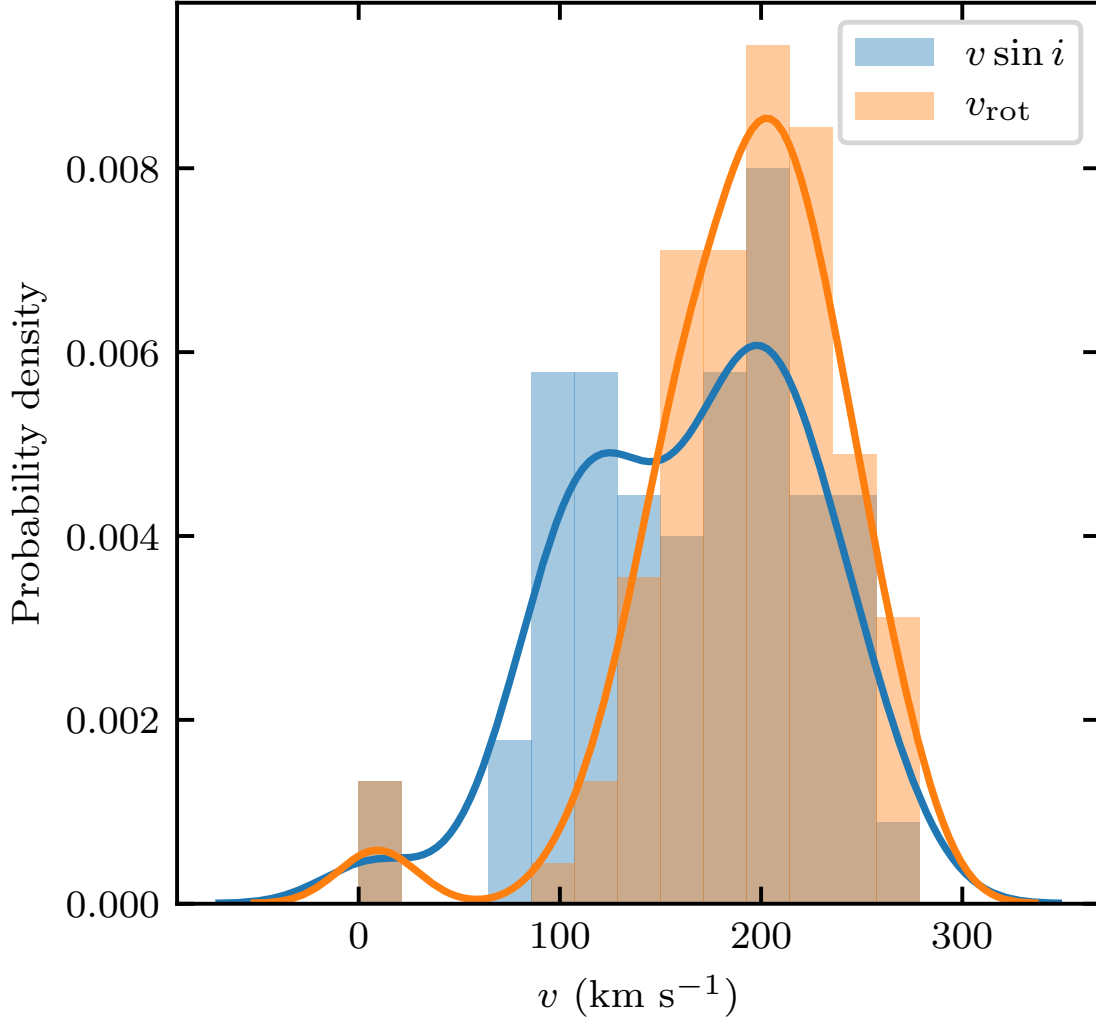


Figure 7. Distributions of projected rotational velocities $v \sin i$ (blue) and true rotational velocities v_{rot} (orange) for member stars in the MSTO region of NGC 5822. Both velocities were estimated by taking the average velocities of the nearest 50 stars in the synthetic CMD.

a similar pattern as the field population in the sense that stars more massive than $2.5 M_{\odot}$ show a bimodal equatorial velocity distribution while less massive stars have a unimodal rotation distribution (Zorec & Royer 2012). However, spin alignment in clusters may play an overlooked role. Corsaro et al. (2017) found evidence of spin alignment among the red giant stars in the two old open clusters NGC 6791 and NGC 6819. Lim et al. (2018) inferred the v_{rot} and the inclination angles i of MSTO stars in NGC 6705 from Monte Carlo simulations where v_{rot} has a linear distribution and i a Gaussian distribution. They argued that cluster members have highly aligned spin axes, which implies a link between stellar rotation and rotational kinetic energy in the progenitor molecular cloud.

We also estimated the stellar masses following similar procedures as Sun et al. (2018). In essence, we generated a synthetic cluster of 10,000 stars with the initial masses generated through Monte Carlo sampling of a Kroupa stellar initial mass function (IMF; Kroupa 2001). Then, we calculated the ratio of the number of member stars with G magnitudes from 12.5 mag to 13.5 mag to that of the synthetic cluster for the same magnitude range. We multiplied the integrated mass obtained for the synthetic cluster by this ratio to estimate the total stellar mass in the cluster, $1.7 \pm 0.3 \times 10^3 M_{\odot}$. We confirmed that changing the magnitude range will not affect the estimation of the total mass significantly. Bastian et al. (2018) reported a mass of $2800 M_{\odot}$ for NGC 2818. These results suggest that eMSTOs are not exclusive to massive clusters ($10^4 - 10^5 M_{\odot}$).

Table 2. Properties of member stars with rotational velocity measurements.

Gaia ID	G (mag)	G_{bp} (mag)	G_{rp} (mag)	T (K) ^a	$\log g$ ^a	Fe/H ^a	$v \sin i$ (km s ⁻¹) ^b	v_{rv} (km s ⁻¹) ^c
(1)	(2)	(3)	(4)	(5)	(6)	(7)	(8)	(9)
5887641469783582208	12.28	12.50	11.92	6900 ± 100	3.5 ± 0.1	0.0 ± 0.5	82.0 ± 12.4	-17.8 ± 5.8
5887666444964220416	11.21	11.38	10.93	7400 ± 100	3.9 ± 0.1	0.0 ± 0.5	182.3 ± 6.1	-30.2 ± 7.0
5887666444964220416*	11.21	11.38	10.93	7200 ± 100	3.6 ± 0.1	0.0 ± 0.5	176.9 ± 6.1	-25.2 ± 5.1
5887669198096568960	12.03	12.27	11.64	6800 ± 100	4.2 ± 0.1	-0.5 ± 0.5	110.8 ± 8.1	-42.0 ± 6.1
5887668648340678784	10.89	11.07	10.61	7200 ± 100	4.4 ± 0.1	0.0 ± 0.5	16.0 ± 38.8	-30.3 ± 6.6
5887642466216028032	11.82	12.02	11.50	7100 ± 100	4.1 ± 0.1	-0.5 ± 0.5	206.2 ± 5.8	-24.1 ± 6.7
5887642466216028032*	11.82	12.02	11.50	7000 ± 100	4.2 ± 0.1	-0.5 ± 0.5	211.3 ± 5.6	-23.1 ± 14.1
5887668575267987840	11.92	12.10	11.61	6900 ± 100	3.7 ± 0.1	-0.5 ± 0.5	163.0 ± 6.1	-26.8 ± 13.6
5887698644394381952	10.65	10.87	10.31	7200 ± 100	3.6 ± 0.1	0.0 ± 0.5	42.7 ± 24.7	-40.1 ± 6.9
5887698644394381952*	10.65	10.87	10.31	7200 ± 100	3.5 ± 0.1	0.0 ± 0.5	53.9 ± 20.3	-33.4 ± 4.4
5887719054073235584	11.07	11.27	10.76	7400 ± 100	4.0 ± 0.1	0.0 ± 0.5	177.6 ± 6.1	-31.6 ± 5.2
5887719054073235584*	11.07	11.27	10.76	7000 ± 100	4.0 ± 0.1	-0.5 ± 0.5	181.7 ± 6.1	-32.9 ± 6.5
5887644935768013056	11.53	11.72	11.21	7400 ± 100	4.1 ± 0.1	0.0 ± 0.5	194.0 ± 6.0	-42.3 ± 5.2
5887644935768013056*	11.53	11.72	11.21	7400 ± 100	4.0 ± 0.1	0.0 ± 0.5	194.2 ± 6.0	-46.4 ± 9.5
5887671255327574144	12.08	12.29	11.75	7000 ± 100	3.5 ± 0.1	0.0 ± 0.5	33.4 ± 29.0	-21.5 ± 6.0
5887695414549752704	10.92	11.13	10.60	7300 ± 100	3.8 ± 0.1	0.0 ± 0.5	120.9 ± 7.3	-36.6 ± 6.6
5887695414549752704*	10.92	11.13	10.60	7200 ± 100	3.7 ± 0.1	0.0 ± 0.5	124.9 ± 7.0	-26.0 ± 6.8
5887718740485998208	11.19	11.43	10.83	7000 ± 100	3.6 ± 0.1	0.0 ± 0.5	246.9 ± 2.4	-27.7 ± 8.6
5887718740485998208*	11.19	11.43	10.83	7100 ± 100	4.3 ± 0.1	-0.5 ± 0.5	239.0 ± 3.5	-33.2 ± 7.7
5887668197310871168	12.04	12.23	11.72	7100 ± 100	3.7 ± 0.1	0.0 ± 0.5	89.0 ± 11.0	15.9 ± 7.1
5887642981611923200	11.66	11.88	11.30	7000 ± 100	4.2 ± 0.1	-0.5 ± 0.5	249.1 ± 2.1	-28.2 ± 6.8
5887642981611923200*	11.66	11.88	11.30	6900 ± 100	3.5 ± 0.1	-0.5 ± 0.5	249.6 ± 2.0	-26.5 ± 9.7
5887722313898780672	12.02	12.22	11.69	7400 ± 100	4.3 ± 0.1	0.0 ± 0.5	120.0 ± 7.3	-31.9 ± 5.2
5887722313898780672*	12.02	12.22	11.69	7300 ± 100	4.1 ± 0.1	0.0 ± 0.5	143.0 ± 6.3	-26.9 ± 8.1
5887671397119565312	12.74	13.04	12.26	6300 ± 100	4.0 ± 0.1	-0.5 ± 0.5	48.2 ± 22.4	-28.6 ± 8.4
5887698296441666688	11.97	12.17	11.64	7400 ± 100	3.9 ± 0.1	0.5 ± 0.5	108.2 ± 8.3	-31.9 ± 5.0
5887698296441666688*	11.97	12.17	11.64	7400 ± 100	3.7 ± 0.1	0.5 ± 0.5	83.7 ± 12.0	-29.3 ± 5.5
5887697987204027264	11.14	11.33	10.85	7400 ± 100	3.8 ± 0.1	0.0 ± 0.5	178.9 ± 6.1	-31.6 ± 8.9
5887697987204027264*	11.14	11.33	10.85	7400 ± 100	3.9 ± 0.1	0.0 ± 0.5	175.1 ± 6.1	-38.0 ± 6.1
5887671534558688640	12.79	13.04	12.38	6500 ± 100	3.7 ± 0.1	-0.5 ± 0.5	138.4 ± 6.4	-21.8 ± 7.8
5887670224535430272	12.26	12.47	11.91	6600 ± 100	3.5 ± 0.1	-0.5 ± 0.5	34.1 ± 28.7	-58.6 ± 8.3
5887671431479631360	12.77	13.02	12.36	6600 ± 100	3.7 ± 0.1	-0.5 ± 0.5	144.0 ± 6.3	-30.3 ± 7.0
5887665895208406272	12.01	12.21	11.66	7000 ± 100	3.9 ± 0.1	-0.5 ± 0.5	201.6 ± 5.9	-32.7 ± 8.1
5887665895208406272*	12.01	12.21	11.66	7000 ± 100	4.4 ± 0.1	-0.5 ± 0.5	202.4 ± 5.9	-42.0 ± 6.7
5887667544475841152	12.14	12.36	11.77	6800 ± 100	4.0 ± 0.1	-0.5 ± 0.5	65.2 ± 16.6	-51.4 ± 4.4
5887642805464232704	12.24	12.45	11.87	7200 ± 100	4.3 ± 0.1	0.5 ± 0.5	86.0 ± 11.6	-14.4 ± 9.7
5887642805464232704*	12.24	12.45	11.87	7000 ± 100	4.3 ± 0.1	0.5 ± 0.5	123.5 ± 7.1	-0.0 ± 13.6

^aUncertainty adopted from the step size of the model grid.^bUncertainty estimated from the mock test.^cUncertainty given by the MCMC procedure.

*Duplicate observation in Programme 2018-1-SCI-006

NOTE—(1) *Gaia* DR2 ID; (2,3,4) Extinction-corrected *Gaia* bands (5) Effective temperature; (6) Surface gravity; (7) Metallicity; (8) Projected rotational velocity; (9) Radial velocity.

One possible source that could also give rise to a broadened MSTO is stellar variability. [Salinas et al. \(2016\)](#) argued that the instability strip intersects with the MSTO region of a cluster with an age of $\sim 1 - 3$ Gyr and can make a significant contribution to the observed eMSTOs. Follow-up observations of NGC 1846 revealed the presence of a group of (mainly δ Scuti) variable stars around the eMSTO region. However, the number fraction of variable stars was not sufficient to produce the observed width of the eMSTO ([Salinas et al. 2018](#)). Certain types of variable or binary stars (e.g., EA-type eclipsing binaries) exhibit large changes in radial velocity over time and can be detected through multi-epoch observations. However, we did not find such candidates in our sample because of the limited spectral resolution and the small number of observations. Follow-up photometric and spectroscopic observations are required to further investigate the role of variability in shaping the morphology of the eMSTO region.

R. d. G. and L. D. acknowledge research support from the National Natural Science Foundation of China through grants 11633005, 11473037, and U1631102. R. d. G. is grateful for support from the National Key Research and Development Program of China through grant 2017YFA0402702 from the Chinese Ministry of Science and Technology (MOST). L. D. also acknowledges support from MOST through grant 2013CB834900.

Facilities: SALT(RSS)

Software: PySALT ([Crawford et al. 2010](#)), PARSEC (1.2S; [Bressan et al. 2012](#)), Astropy ([Astropy Collaboration et al. 2013](#)), Matplotlib ([Hunter 2007](#)), SYNSPEC ([Hubeny & Lanz 1992](#)), emcee ([Foreman-Mackey et al. 2013](#))

REFERENCES

- Astraatmadja, T. L., & Bailer-Jones, C. A. L. 2016, *ApJ*, 832, 137
- Astropy Collaboration, Robitaille, T. P., Tollerud, E. J., et al. 2013, *A&A*, 558, A33
- Bastian, N., Cabrera-Ziri, I., Niederhofer, F., et al. 2017, *MNRAS*, 465, 4795
- Bastian, N., & de Mink, S. E. 2009, *MNRAS*, 398, L11
- Bastian, N., Kamann, S., Cabrera-Ziri, I., et al. 2018, *MNRAS*, 480, 3739
- Brandt, T. D., & Huang, C. X. 2015a, *ApJ*, 807, 58
- Brandt, T. D., & Huang, C. X. 2015b, *ApJ*, 807, 25
- Brandt, T. D., & Huang, C. X. 2015c, *ApJ*, 807, 24
- Bressan, A., Marigo, P., Girardi, L., et al. 2012, *MNRAS*, 427, 12
- Buckley, D. A. H., Swart, G. P., & Meiring, J. G. 2006, *SPIE Conf. Ser.*, 6267, 62670Z
- Cantat-Gaudin, T., Jordi, C., Vallenari, A., et al. 2018, *A&A*, 618, A93
- Cardelli, J. A., Clayton, G. C., & Mathis, J. S. 1989, *ApJ*, 345, 245
- Carraro, G., Anthony-Twarog, B. J., Costa, E., et al. 2011, *AJ*, 142, 127
- Claret, A. 2000, *A&A*, 359, 289
- Cordoni, G., Milone, A. P., Marino, A. F., et al. 2018, *ApJ*, 869, 139
- Correnti, M., Goudfrooij, P., Bellini, A., et al. 2017, *MNRAS*, 467, 3628
- Corsaro, E., Lee, Y.-N., García, R. A., et al. 2017, *Nat. Astron.*, 1, 64
- Crawford, S. M., Still, M., Schellart, P., et al. 2010, *Observatory Operations: Strategies, Processes, and Systems III*, 773725
- Dias, W. S., Alessi, B. S., Moitinho, A., et al. 2002, *A&A*, 389, 871
- Dupree, A. K., Dotter, A., Johnson, C. I., et al. 2017, *ApJL*, 846, L1
- Espinosa Lara, F., & Rieutord, M. 2011, *A&A*, 533, A43
- Foreman-Mackey, D., Hogg, D. W., Lang, D., et al. 2013, *PASP*, 125, 306
- Gaia Collaboration, Brown, A. G. A., Vallenari, A., et al. 2018, *A&A*, 616, A1
- Gaia Collaboration, Prusti, T., de Bruijne, J. H. J., et al. 2016, *A&A*, 595, A1
- Georgy, C., Charbonnel, C., Amard, L., et al. 2018, *A&A*, 622, A66
- Georgy, C., Ekström, S., Granada, A., et al. 2013, *A&A*, 553, A24
- Georgy, C., Granada, A., Ekström, S., et al. 2014, *A&A*, 566, A21
- Goudfrooij, P., Puzia, T. H., Kozhurina-Platais, V., et al. 2011, *ApJ*, 737, 3
- Huang, W., & Gies, D. R. 2006, *ApJ*, 648, 580
- Huang, W., Gies, D. R., & McSwain, M. V. 2010, *ApJ*, 722, 605
- Hubeny, I., & Lanz, T. 1992, *A&A*, 262, 501

- Hunter, J. D. 2007, *Computing in Science and Engineering*, 9, 90
- Kamann, S., Bastian, N., Husser, T.-O., et al. 2018, *MNRAS*, 480, 1689
- Kroupa, P. 2001, *MNRAS*, 322, 231
- Kurucz, R. L. 2005, *Mem. Soc. Astron. It. Suppl.*, 8, 189
- Li, C., de Grijs, R., & Deng, L. 2014a, *Nature*, 516, 367
- Li, C., de Grijs, R., & Deng, L. 2014b, *ApJ*, 784, 157
- Lim, B., Rauw, G., Nazé, Y., et al. 2018, *Nat. Astron.*, 156
- Mackey, A. D., & Broby Nielsen, P. 2007, *MNRAS*, 379, 151
- Mackey, A. D., Broby Nielsen, P., Ferguson, A. M. N., et al. 2008, *ApJL*, 681, L17
- Marino, A. F., Milone, A. P., Casagrande, L., et al. 2018a, *ApJL*, 863, L33
- Marino, A. F., Przybilla, N., Milone, A. P., et al. 2018b, *AJ*, 156, 116
- Milone, A. P., Bedin, L. R., Piotto, G., et al. 2009, *A&A*, 497, 755
- Milone, A. P., Bedin, L. R., Piotto, G., et al. 2015, *MNRAS*, 450, 3750
- Milone, A. P., Marino, A. F., D’Antona, F., et al. 2016, *MNRAS*, 458, 4368
- Nataf, D. M., Gould, A., Fouqué, P., et al. 2013, *ApJ*, 769, 88
- Niederhofer, F., Georgy, C., Bastian, N., et al. 2015, *MNRAS*, 453, 2070
- O’Donnell, J. E. 1994, *ApJ*, 422, 158
- Palacios, A., Gebran, M., Josselin, E., et al. 2010, *A&A*, 516, A13
- Salinas, R., Pajkos, M. A., Strader, J., et al. 2016, *ApJL*, 832, L14
- Salinas, R., Pajkos, M. A., Vivas, A. K., et al. 2018, *AJ*, 155, 183
- Schlafly, E. F., & Finkbeiner, D. P. 2011, *ApJ*, 737, 103
- Sun, W., Li, C., de Grijs, R., et al. 2018, *ApJ*, 862, 133
- Yang, W., Bi, S., Meng, X., et al. 2013, *ApJ*, 776, 112
- Zacharias, N., Urban, S. E., Zacharias, M. I., et al. 2000, *AJ*, 120, 2131
- Zorec, J., & Royer, F. 2012, *A&A*, 537, A120